Electronic Supplementary Material (ESI) for Journal of Materials Chemistry B.

Supporting Information

PtCo Bimetallic Nanoparticles with High Oxidase-like Catalytic Activity and Their Applications for Magnetic-enhanced Colorimetric Biosensing

Shuangfei Cai [-],[a], *Cui Qi* [-], [a], *Yadong L i* [b], *Qiusen Han*[a], *Rong Yang**,[a], *Chen Wang**,[a]

[a] CAS Key Lab for Biological Effects of Nanomaterials and Nanosafety, National Center for Nanoscience and Technology, Beijing 100190, P. R. China

[b] Department of Chemistry, Tsinghua University, Beijing, 100084, China

* Corresponding authors: yangr@nanoctr.cn and wangch@nanoctr.cn

[-] These authors contributed equally to this work.

Table S1. Usage of precursors for the synthesis of Pt_xCo_{100-x} nanoparticles.

Entry	Nanoparticles	$Pt(acac)_2$ (mg)	$Co(acac)_2$ (mg)
1	Pt	8	-
2	$Pt_{98}Co_2$	8	1.3
3	$Pt_{90}Co_{10}$	8	2.6
4	$Pt_{81}Co_{19}$	8	5.1
5	$Pt_{72}Co_{28}$	8	10.2
6	$Pt_{33}Co_{67}$	8	20.4

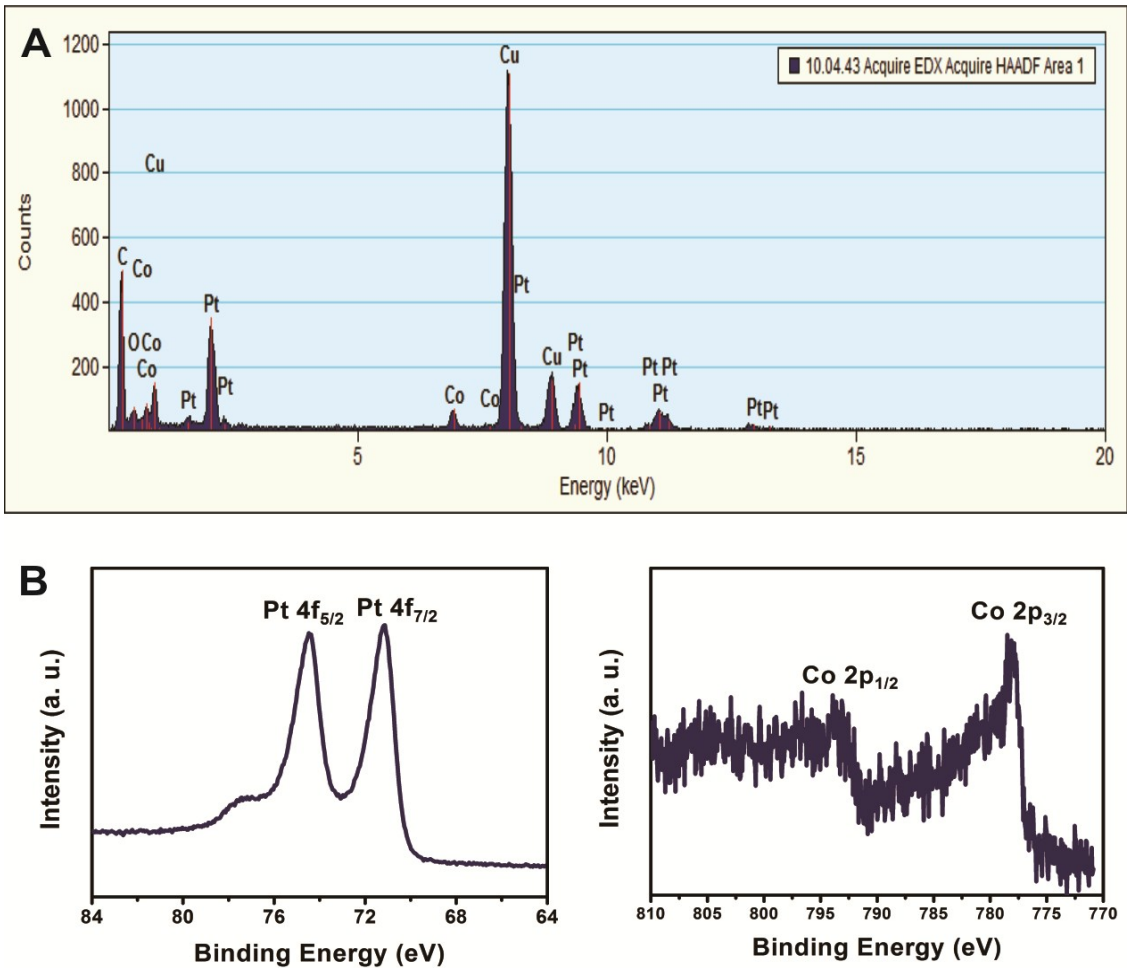

Fig. S1. (a) EDX spectrum of as-prepared $Pt_{72}Co_{28}$ NPs. The Cu peaks resulted from the sample grid. (b) XPS for $Pt_{72}Co_{28}$ NPs, Pt 4f region, and Co 2p region of $Pt_{72}Co_{28}$ NPs.

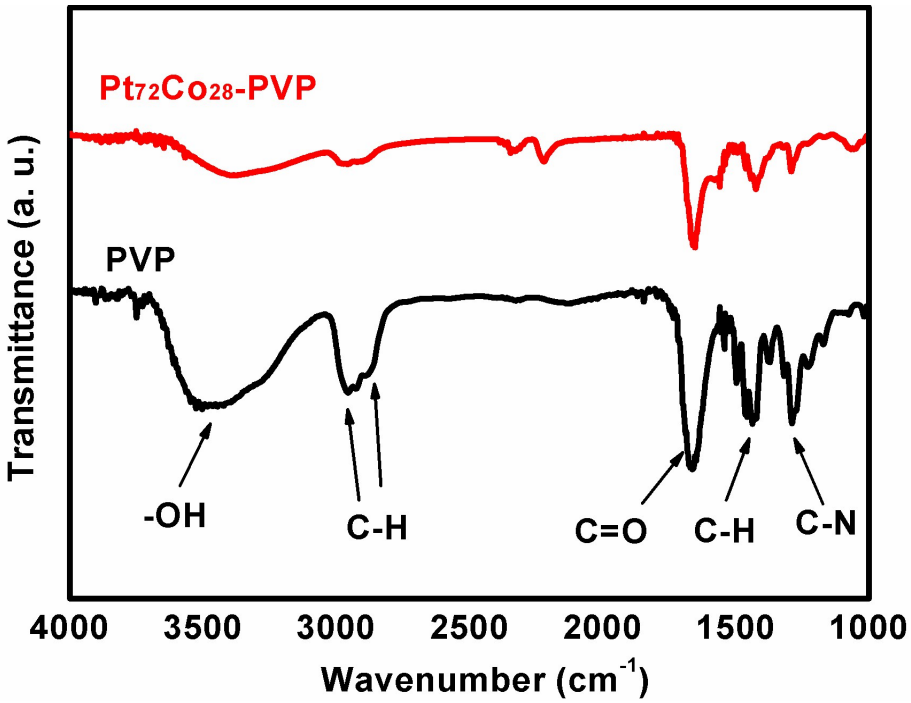

Fig. S2. FT-IR spectra of PVP and as-prepared $Pt_{72}Co_{28}$ NPs.

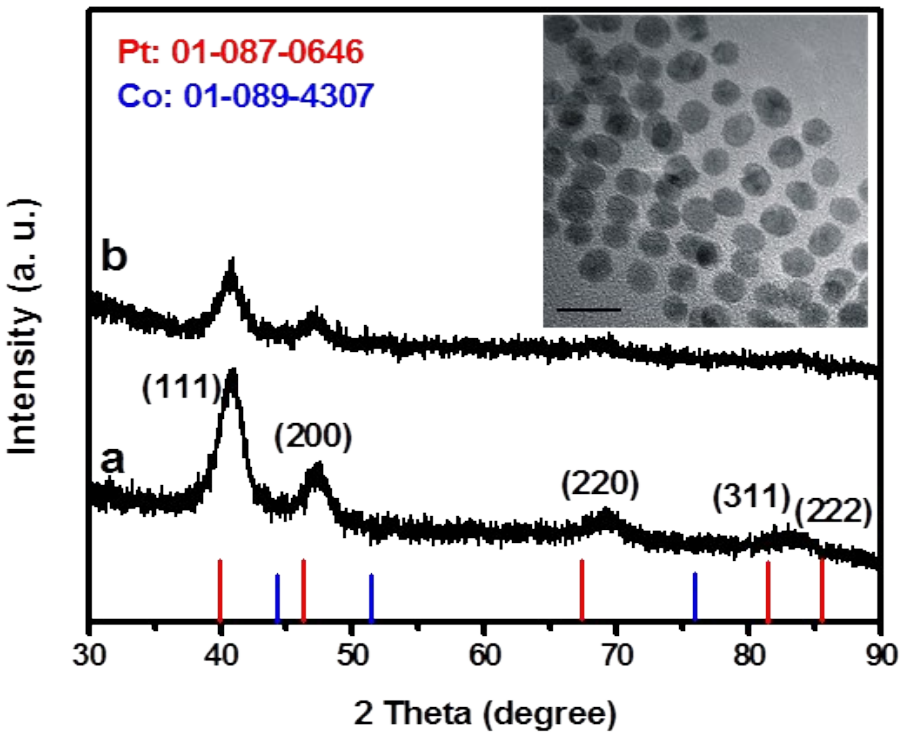

Fig. S3. XRD patterns of (a) the Pt72Co28 NPs and (b) the sample after treatment with concentrated HCl (inset showed the TEM image, scale bar: 10 nm).

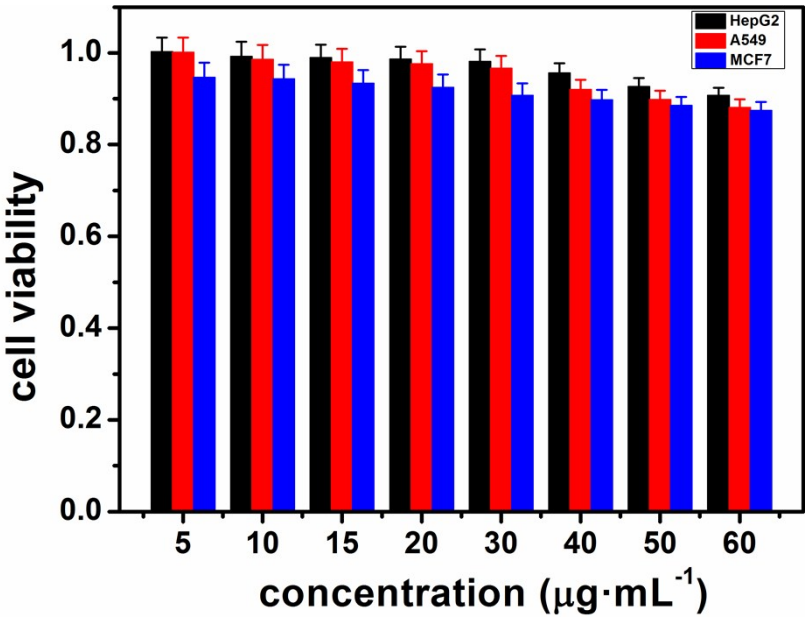

Fig. S4. Cytotoxicity of $Pt_{72}Co_{28}$ NPs on HepG2, A549 and MCF-7 cells was determined by CCK-8 assays after incubation NPs with cells for 48 h. The data were shown as the mean value and standard deviation and the experiments were performed in triplicate.

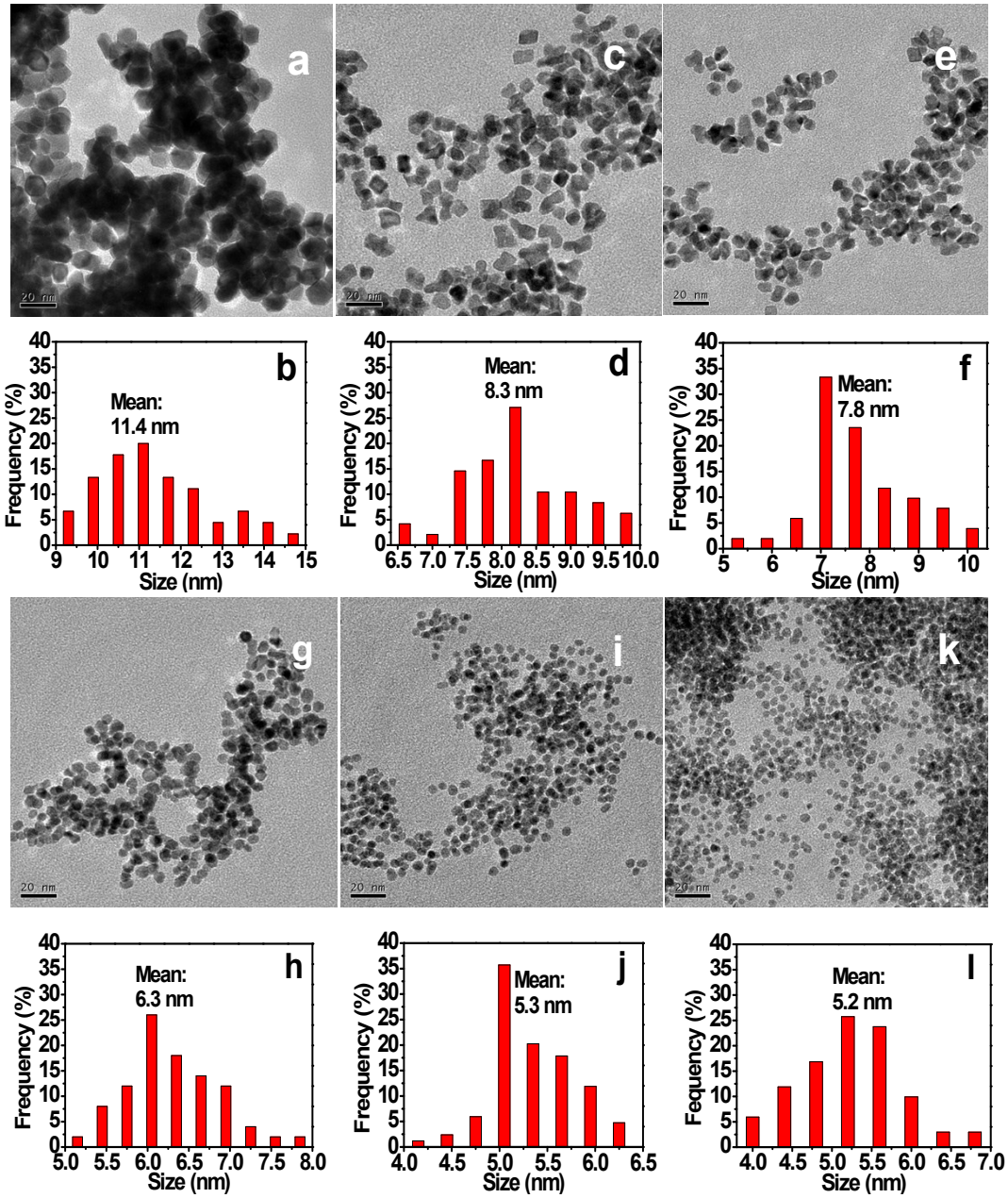

Fig. S5. Representative TEM images and statistic diameters of as-prepared NPs: (a, b) Pt, (c, d) $Pt_{98}Co_2$, (e, f) $Pt_{90}Co_{10}$, (g, h) $Pt_{81}Co_{19}$, (i, j) $Pt_{72}Co_{28}$ and (k, l) $Pt_{33}Co_{67}$.

Fig. S5 showed the as-prepared Pt and Pt-Co NPs were monodisperse and uniform in size. The as-prepared Pt NPs was octahedral in shape with an average diameter of 11.4 nm from one apex to the opposite apex (Fig. S5a). As the Co content increased, however, the morphology of Pt-Co NPs changed gradually from octahedral to near-spherical (Fig. S5a to S5l) with a narrow size distribution.

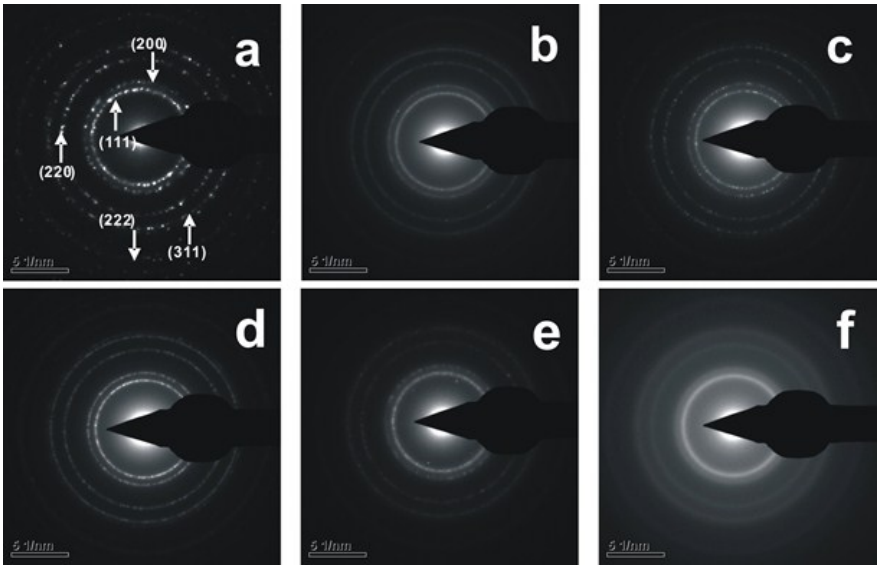

Fig. S6. SAED patterns of as-prepared NPs: (a) Pt, (b) $Pt_{98}Co_2$, (c) $Pt_{90}Co_{10}$, (d) $Pt_{81}Co_{19}$, (e) $Pt_{72}Co_{28}$ and (f) $Pt_{33}Co_{67}$.

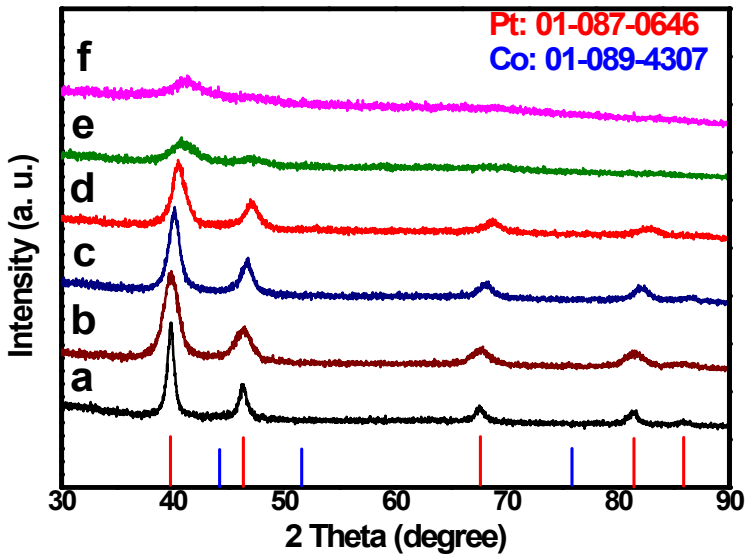

Fig. S7. XRD patterns of as-prepared NPs: (a) Pt, (b) $Pt_{98}Co_2$, (c) $Pt_{90}Co_{10}$, (d) $Pt_{81}Co_{19}$, (e) $Pt_{72}Co_{28}$ and (f) $Pt_{33}Co_{67}$.

The XRD patterns in Fig. S7 could be indexed to {111}, {200}, {220}, {311} and {222} diffractions of a fcc structure of Pt-Co NPs. With an increase in the Co content, the peaks of Pt_xCo_{100-x} NPs continuously shifted from Pt standard peaks (red line) to Co (blue line), which could be ascribed to the decreased lattice spacing resulting in the replacement of Pt atoms by smaller Co atoms.

The effect of time on the growth of $Pt_{72}Co_{28}$ NPs

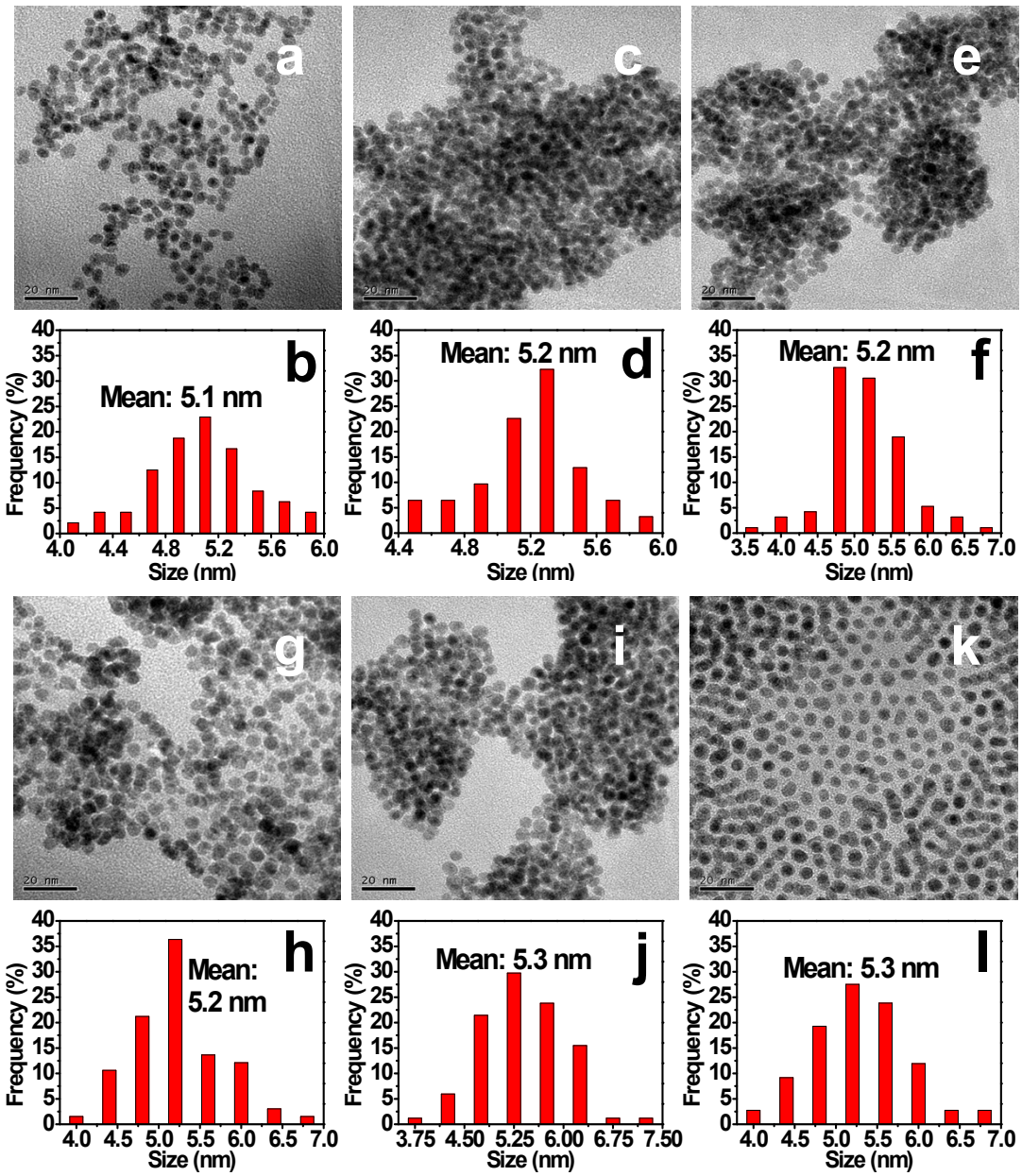

Fig. S8. TEM images and statistic diameters of the products collected at (a and b) 1 h, (c and d) 2 h, (e and f) 4 h, (g and h) 6 h, (i and j) 8 h and (k and l) 12 h, respectively.

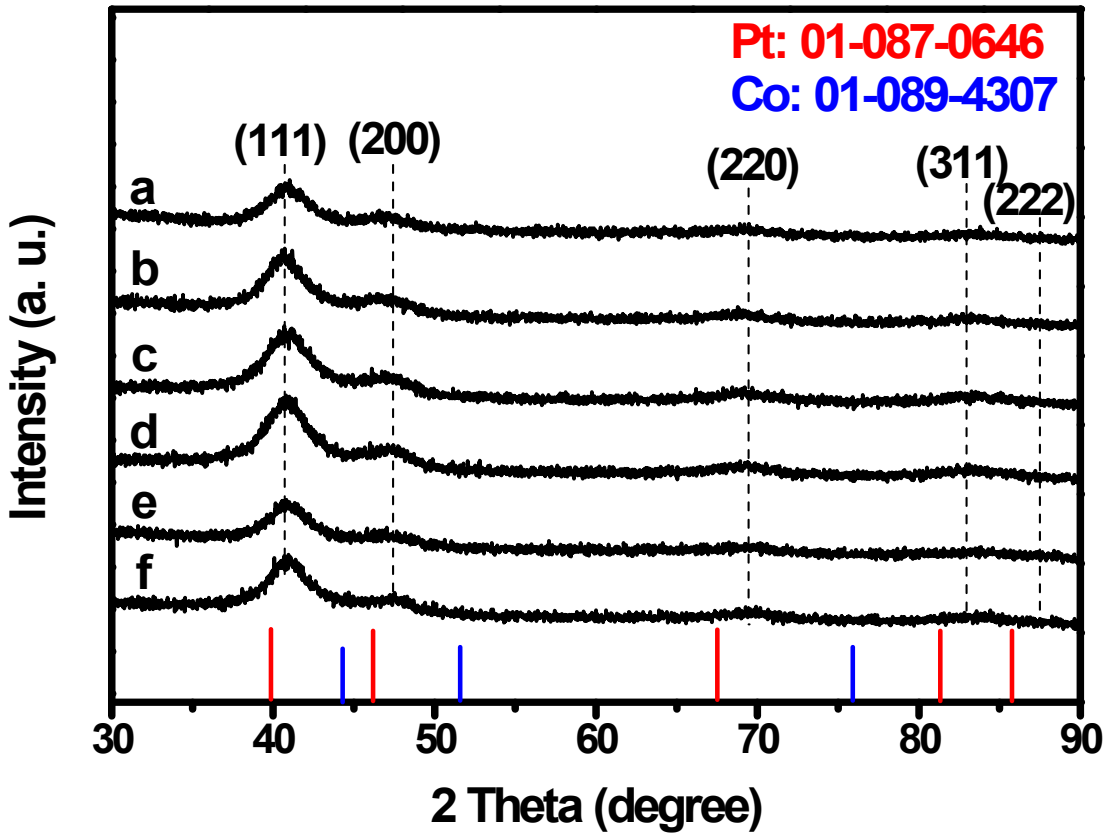

Fig. S9. XRD patterns of the products collected at (a) 1 h, (b) 2 h, (c) 4 h, (d) 6 h, (e) 8 h and (f) 12 h, respectively.

For the $Pt_{72}Co_{28}$ NPs, the time sequential evolution experiments using $Pt(acac)_2$ and $Co(acac)_2$ as precursors at 180 °C were studied and the TEM data were collected at different reaction time. The results showed that the formation of the near-spherical NPs with the size of 5.1 nm after 1 h of reaction time (Fig. S8a and S8b). With the increase in reaction time, the products had no significant change in size and still near-spherical shape (Fig. S8c-S8l) as well as XRD patterns (Fig. S9), indicating the stable crystalline structure formed during the short reaction time. A same atomic ratio of Pt/Co (72:28) for the products collected at different reaction time was obtained by the ICP-OES measurements, verifying the XRD observation.

The effect of temperature on the growth of $Pt_{72}Co_{28}$ NPs

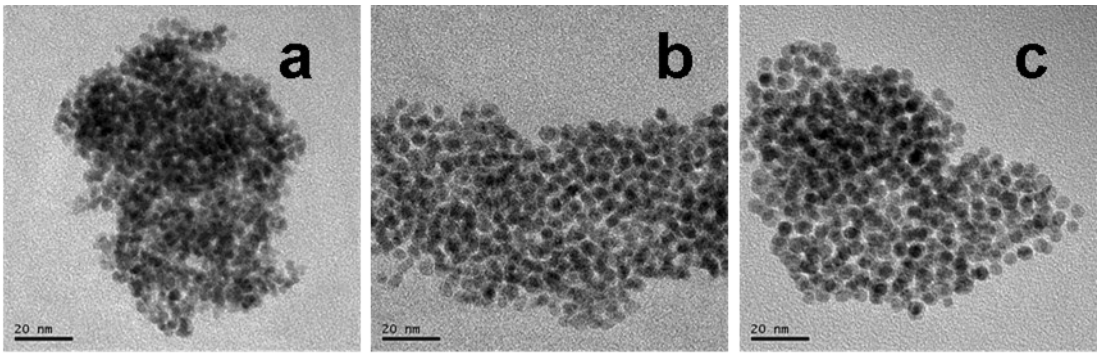

Fig. S10. The effect of temperature on the morphology and size of products obtained by the reduction of $Pt(acac)_2$ and $Co(acac)_2$ for the $Pt_{72}Co_{28}$ sample in the presence of benzoic acid ((a) 120 ^oC, (b) 150 ^oC, (c) 210 ^oC).

For the $Pt_{72}Co_{28}$ NPs, the effect of reaction temperature on the morphology and size of products was studied. The experimental time was 12 h. If the reaction was conducted at 120 ^oC, as shown in Figure S10a, only a little product was obtained (< 15 %) and the mean diameter was smaller than 4 nm. It could be explained that benzyl alcohol is a weak reducing agent, so it is difficult to reduce Pt^{2+} to Pt^0 at low temperature. As the temperature increased, the products had a slight increase in size and still near-spherical in shape (Fig. S10b to S10c).

The effect of Co precursors on the growth of $Pt_{72}Co_{28}$ NPs

To further investigate the effect of different metal precursors, $Co(acac)_2$ was replaced with three different Co ion precursors: $Co(OAc)_2 \cdot 4H_2O$, $CoCl_2 \cdot 6H_2O$ and $Co(NO_3)_2 \cdot 6H_2O$. The products were still near-spherical in shape and had a little change in size in the range of 5.8 to 8.3 nm (Fig. S11a to S11c), which suggested the employment of different Co^{2+} as precursors could be efficient in our system.

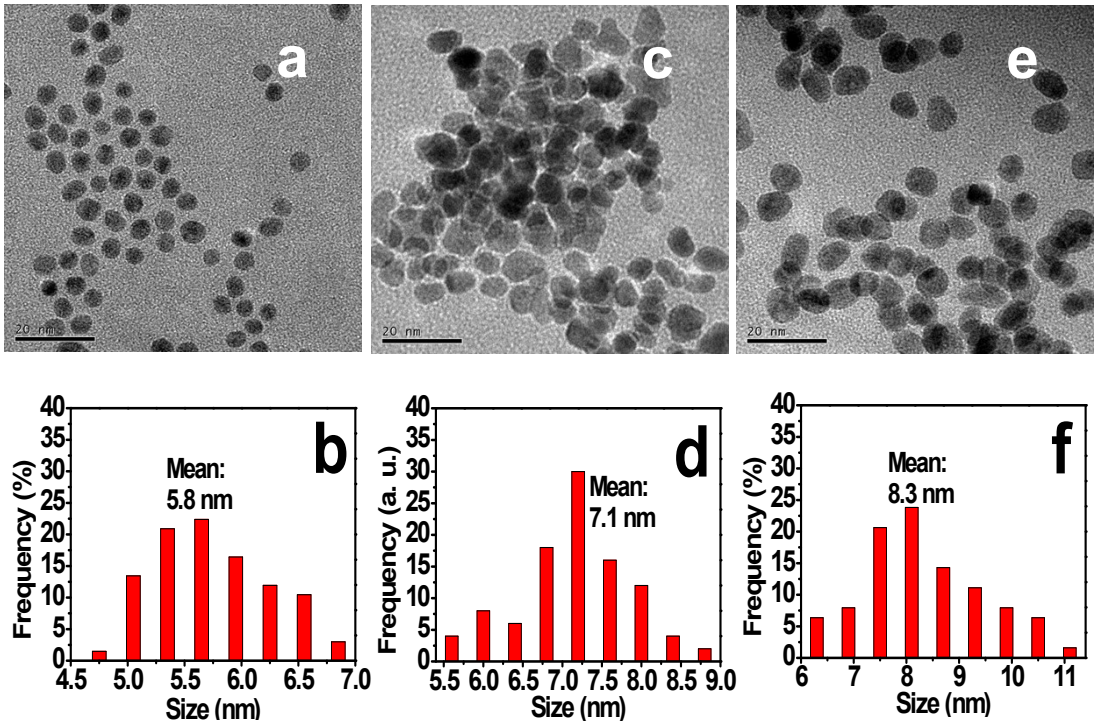

Fig. S11. Representative TEM images and statistic diameters of as-prepared NPs by the reduction of $Pt(acac)_2$ and different Co salt precursors: (a, b) $Co(OAc)_2 \cdot 4H_2O$, (c, d) $CoCl_2 \cdot 6H_2O$ and (e, f) $Co(NO_3)_2 \cdot 6H_2O$.

However, there was a slight change in the XRD patterns of products (Fig. S12), indicating the subtle difference in the composition from each other. Above results suggested that the temperature, reducing agent, nucleation inhibitor and metal precursors played an important role on the shape, size and composition of Pt_xCo_{100-x} NPs.

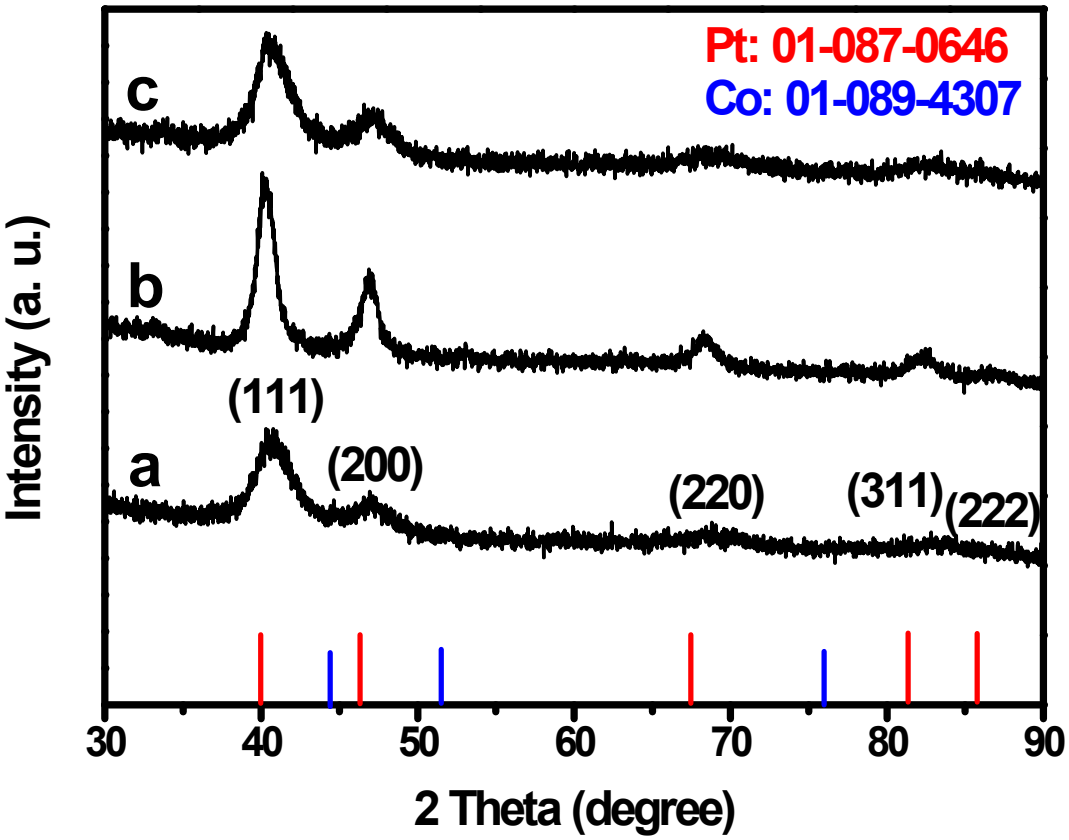

Fig. S12. XRD patterns of the as-prepared NPs obtained by the reduction of $Pt(acac)_2$ and different Co salt precursors at 180 °C for 12 h: (a) $Co(OAc)_2 \cdot 4H_2O$, (b) $CoCl_2 \cdot 6H_2O$ and (c) $Co(NO_3)_2 \cdot 6H_2O$.

Growth mechanism

It is widely accepted that the evolution of nanocrystals in a solution system consists of a nucleation stage and subsequent Ostwald ripening growth on the existing seeds (or nuclei).[1-3] Based on above results, the proposed mechanism for the formation of Pt_xCo_{100-x} NPs was as follows. First, Pt species with higher redox potential were reduced to octahedral Pt nanocrystals as seeds in the presence of benzoic acid. At high temperature, the PVP molecules on the surface of octahedral Pt seeds could desorb, leaving active sites on the Pt surface. Thus, Co ions were randomly adsorbed on the surface of octahedral Pt seeds and subsequently reduced. Then, the newly produced highly reactive Co atoms or clusters collided with active sites of Pt NPs and quickly diffused from the surface into the crystal lattice of Pt seeds. The reduction and diffusion process proceeded continuously, leading to the formation of Pt_xCo_{100-x} NPs.

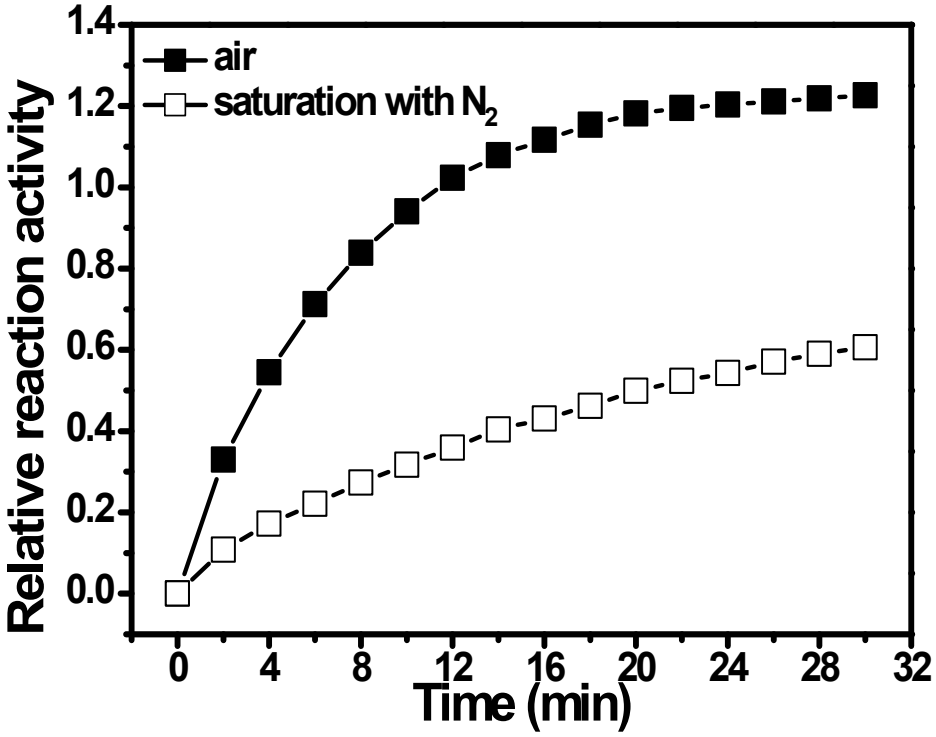

Fig. S13. Effect of dissolved oxygen or saturation with N_2 on TMB oxidation.

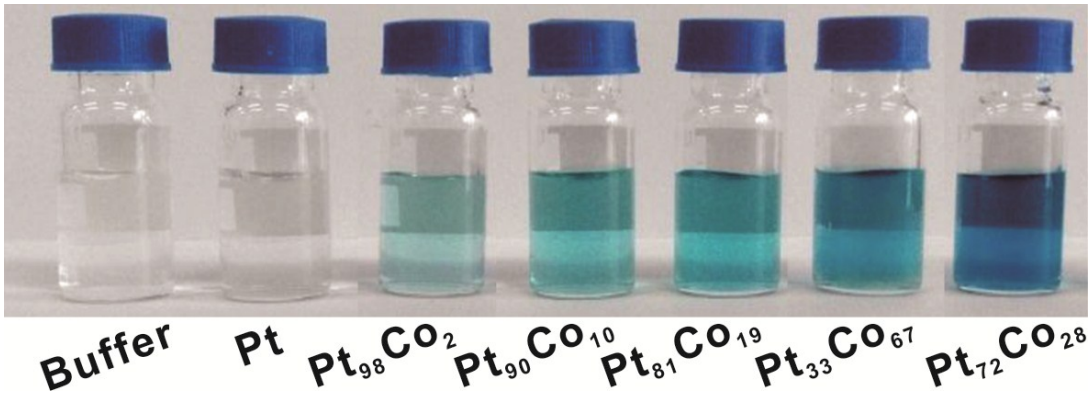

Fig. S14. The color change for the catalyzed oxidation of TMB by Pt-Co NPs with different Pt/Co ratios, which is corresponding to the UV-Vis spectra in Figure 3B. The molar amount of metals in each solution was kept constant.

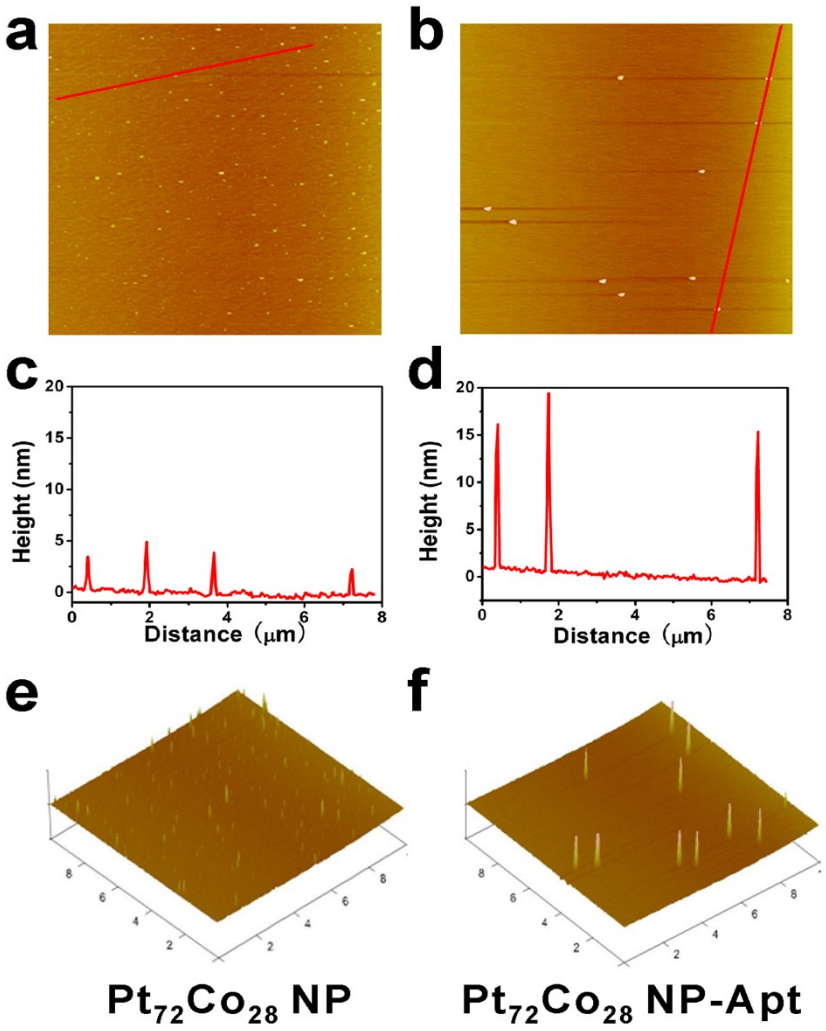

Fig. S15. Top view AFM images (a, b), line profiles(c, d) and surface plots (e, f) of $Pt_{72}Co_{28}$ NPs and $Pt_{72}Co_{28}$-Apt conjugates, respectively.

Table S2. Zeta potential of the as-prepared $Pt_{72}Co_{28}$ NPs, $Pt_{72}Co_{28}$-SA and $Pt_{72}Co_{28}$-Apt in water (pH 6.5) at 25 °C.

Nanocomposite	Zeta potential (mV)
$Pt_{72}Co_{28}$	-13.3 ± 0.4
$Pt_{72}Co_{28}$-SA	-15.7 ± 1.3
$Pt_{72}Co_{28}$-Apt	-28.1 ± 0.7

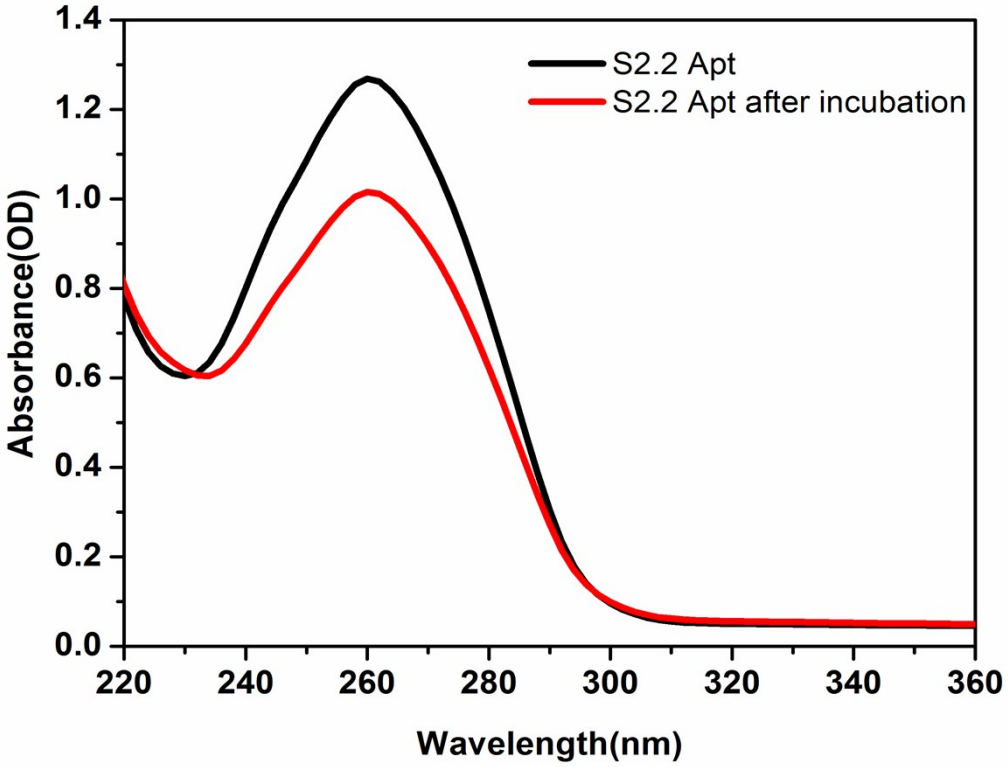

Fig. S16. UV-Vis absorption spectra of S2.2 aptamers and free S2.2 aptamers in the supernatants after centrifugation of the $Pt_{72}Co_{28}$-Apt nanoconjugate solution, respectively.

The loading capacity of aptamers was determined by UV spectra at 260 nm (Fig. S16). It was calculated by measuring the amount of unloaded aptamers in the supernatant after purification of the $Pt_{72}Co_{28}$ nanocnonjugates by centrifugation. The results showed that about two aptamer molecules were labeled on per NP. Please see the detailed calculation as follows:

(1) The number of $Pt_{72}Co_{28}$ NPs in the solution:

From TEM image (Fig. 2A), the morphology of $Pt_{72}Co_{28}$ alloy NPs is almost spherical. Each $Pt_{72}Co_{28}$ NP is composed of both Pt and Co atoms. Accordingly, a sphere model was used to estimate the number of NPs.

The diameter of each $Pt_{72}Co_{28}$ NP is 5.3 nm, so the volume of each $Pt_{72}Co_{28}$ NP is:

$$\frac{4 \times \pi \times \left(\frac{5.3}{2}\right)^3}{3} = 77.95\ nm^3$$

From the HRTEM image (Figure 2B) and XRD pattern (Figure 2C), $Pt_{72}Co_{28}$ NP has the face-centered-cubic (fcc) structure and the distance of two {111} facet is 0.221 nm, then the volume of a unit cell is:

$$(0.221 \times \frac{\sqrt{3}}{2} \times 2)^3 = 0.056\ nm^3$$

Since each unit cell for fcc structure contains 4 apex atoms, the total number of atoms in a single $Pt_{72}Co_{28}$ NP is

$$\frac{4 \times 77.95}{0.056} = 5568$$

According to the ICP-OES result, the Pt and Co content in 1 mL of $Pt_{72}Co_{28}$ dispersion was 317.2 and 36.4 μg, respectively. Hence, the total metal content (Pt + Co) of 1 mL of $Pt_{72}Co_{28}$ dispersion is:

$$\frac{317.2}{195.08} + \frac{36.4}{58.93} = 2.2\ \mu mol$$

Avogadro constant is 6.022×10^{23} mol^{-1}, so the number of NPs is:

$$\frac{(2.2 \times 10^{-6}) \times (6.022 \times 10^{23})}{5568} = 2.4 \times 10^{14}$$

(2) The loading of aptamer molecules on $Pt_{72}Co_{28}$ NPs:

The loading capacity of aptamers was determined by UV spectra at 260 nm (Fig. S16). It was calculated by measuring the amount of unloaded aptamers in the

supernatant after purification of the $Pt_{72}Co_{28}$ nanocnonjugates by centrifugation. The amount of S2.2 aptamer labeled on $Pt_{72}Co_{28}$ NPs was 0.675 nmol. So, the loading of S2.2 aptamer molecules on NPs can be calculated as follows:

$$\frac{number\ of\ Apt\ molecules}{number\ of\ NPs} = \frac{(0.675 \times 10^{-9}) \times (6.022 \times 10^{23})}{2.4 \times 10^{14}} = 1.69$$

There are about two aptamer molecules conjugated to each $Pt_{72}Co_{28}$ NP.

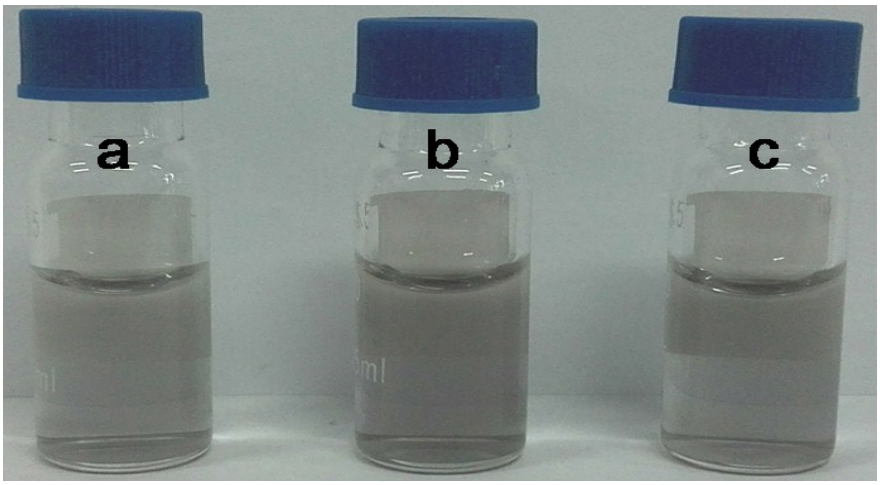

Fig. S17. Photos of (a) $Pt_{72}Co_{28}$ NPs, (b) $Pt_{72}Co_{28}$-SA and (c) $Pt_{72}Co_{28}$-Apt in PBS. They show good dispersibilities.

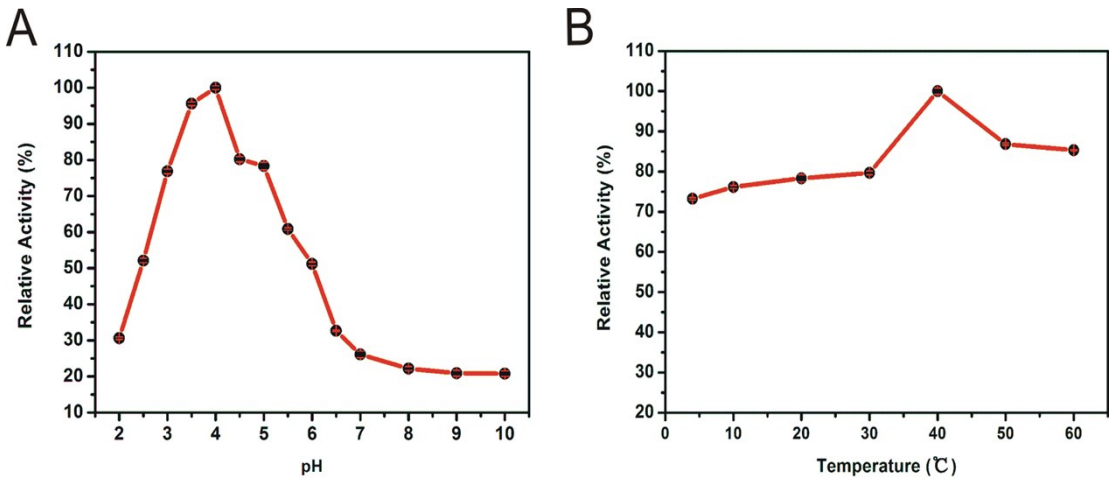

Fig. S18. The catalytic activity of $Pt_{72}Co_{28}$-Apt nanoconjugates was dependent on pH (A) and temperature (B). Reaction conditions: 5 μL of of TMB (60 μM), 5 μL of $Pt_{72}Co_{28}$-Apt nanoconjugates.

For the catalytic oxidation of TMB by nanoconjugates in phosphate buffer, the optimal optimal temperature is 40 °C and the pH value is 4.0. In addition, the effect of the temperature on the catalytic activity of nanoconjugates was smaller than that of pH value. The oxidase activity of nanoconjugates remained about 75 % even at 4 °C compared to that at 40 °C. The high oxidase activity of the nanoconjugates in a broad temperature range demonstrated that it is a promising candidate for colorimetric biosensing.

There are several factors may affect the catalysis efficiency, such as the stability of NPs which depends on the surface electrostatic potential, particle size and the effect of ion type and concentration, *etc*. In our experiments, the optimal pH value is 4.0. $Pt_{72}Co_{28}$ NPs are initially dispersed in PBS (pH 7.4) to give a stock solution, which are negatively charged.

(1) When pH value is low (pH < 4), owing to the existence of large amounts of electrolytic ions (H^+), potential barrier between particles is impaired and NPs tends to

be unstable. Adjusting pH from 1 to 4 by the addition of OH^-, a portion of H^+ ions are neutralized and the potential barrier between particles can be enhanced, which prevents particles from contacting one another to aggregate. The stability of NPs recovers, and hence the catalysis efficiency recovers.

(2) When pH value is > 4, the solubility of TMB decreased. The TMB molecule has a structure of diamine, which results in poor solubility of TMB in a base media. Accordingly, the conversion of oxidation reaction of TMB becomes slow by increasing pH over 4.0. When pH is > 7, PVP molecule tends to be unstable, since the nucleophilic attack of OH^- to the carbonyl group of PVP molecule results in the hydrolysis reaction of PVP, giving rise to the aggregation and deactivation of NPs.

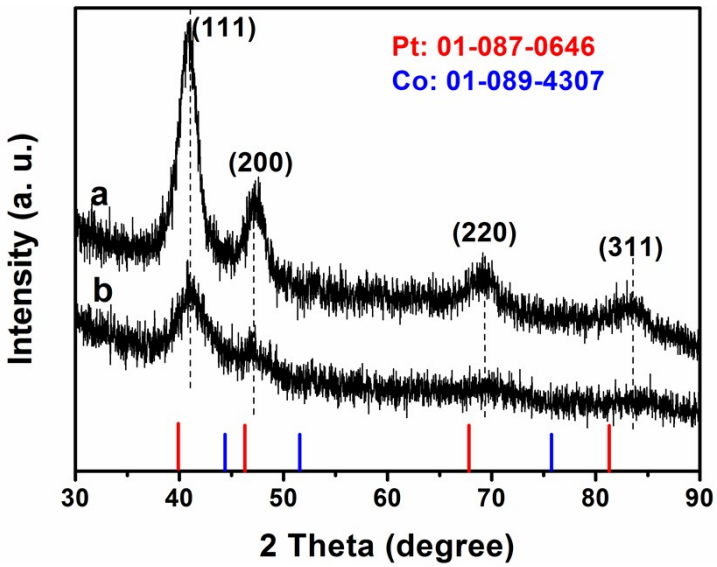

Fig. S19. XRD patterns of (a) the $Pt_{72}Co_{28}$ NPs and (b) the sample after treatment with 2 M H_2SO_4. No apparent change in the crystalline structure of $Pt_{72}Co_{28}$ NPs was observed after the treatment with H_2SO_4 solution.

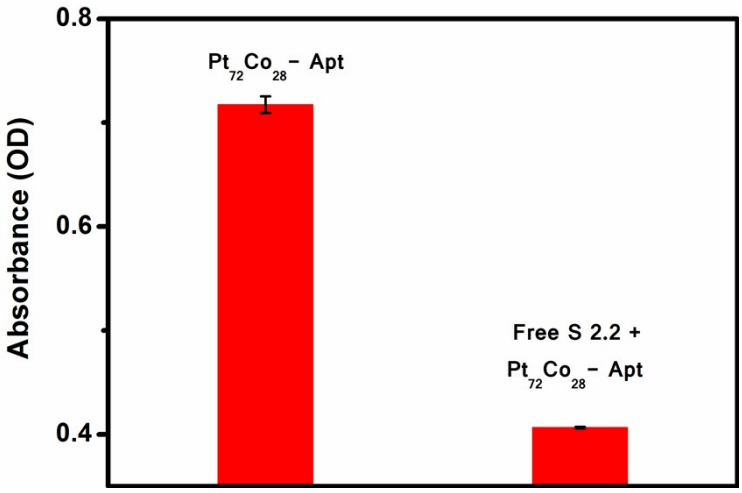

Fig. S20. Binding abilities of $Pt_{72}Co_{28}$-Apt to MCF-7 with and without free S2.2 aptamers.

References:

1 Y. Wu, S. Cai, D. Wang, W. He, Y. Li, *J. Am. Chem. Soc.* 2012, **134**, 8975-8981.

2 Y. Xiong, Y. Xia, *Adv. Mater.* 2007, **19,** 3385-3391;

3 C. B. Murray, C. R. Kagan, M. G. Bawendi, *Annu. Rev. Mater. Sci.* 2000, **30**, 545-610.